Magnetic instability under ferroaxial moment

Akane Inda and Satoru Hayami
Faculty of Science, Hokkaido University, Sapporo 060-0810, Japan

(Received 4 December 2023; accepted 30 April 2024; published 13 May 2024)

Magnetic anisotropy is one of the important factors in determining magnetic structures. The type of magnetic anisotropy is closely related to the symmetry of crystals. We theoretically investigate magnetic anisotropy and its related magnetic instability arising from an electric axial moment, which appears under the breaking of the mirror symmetry parallel to the moment but does not require the breakings of both spatial inversion and time-reversal symmetries. By performing perturbation and mean-field calculations in a complementary way, we show the appearance of the in-plane magnetic anisotropy when the electric axial moment occurs, which tends to tilt in-plane spin moments from the crystal axes in collaboration with relativistic spin-orbit coupling. We demonstrate such a tendency for single-sublattice and four-site cluster models. In the four-site cluster model, we show that a spin configuration consisting of magnetic monopole and magnetic toroidal dipole tends to be realized in the region where a spin vortex is stabilized by the exchange interactions.

DOI: 10.1103/PhysRevB.109.174424

I. INTRODUCTION

The stability of magnetic structures has long been studied in lots of materials. Depending on the types of magnetic interactions and anisotropy, noncollinear and noncoplanar magnetic structures as well as collinear ferromagnetic and antiferromagnetic structures can be realized. The appearance of magnetic anisotropy is often related to the symmetry of the crystal, where the interplay between the relativistic spin-orbit coupling (SOC) and crystalline electric field plays an important role. For example, the Dzyaloshinskii-Moriya (DM) interaction is present when the spatial inversion symmetry at the bond center is lost [1,2], which favors a helical spiral state and skyrmion crystal [3]. Another example is the Kitaev-type exchange interaction that arises from the strong SOC for the discrete rotational symmetry [4,5], which induces noncoplanar spin textures [6–8]. The relation between magnetic interactions and crystal symmetry has been so far classified in real space [9,10] and momentum space [11]. The complicated magnetic textures induced by magnetic anisotropy lead to unconventional physical phenomena, such as the topological Hall effect under noncoplanar spin textures [12–15] and nonlinear longitudinal/transverse transport under noncollinear/noncoplanar spin textures [16–19].

In the present study, we investigate the origin and the role of magnetic anisotropy under an electric axial moment, whose uniform component is referred to as the ferroaxial (or ferrorotational) moment. The ferroaxial moment corresponds to a time-reversal-even axial dipole moment, which appears when the mirror symmetry parallel to the moment is lost but remains spatial inversion ($\mathcal{P}$) and time-reversal ($\mathcal{T}$) symmetries [20]. The ordered state of such a ferroaxial moment has been experimentally observed in materials like $CaMn_7O_{12}$ [21], $RbFe(MoO_4)_2$ [22,23], $NiTiO_3$ [24,25], $Ca_5Ir_3O_{12}$ [26–29], and $BaCoSiO_4$ [30]. Although the ferroaxial moment does not directly couple to neither electric field nor magnetic field owing to the even parity in terms of the $\mathcal{P}$ and $\mathcal{T}$ symmetries, recent studies clarified that it becomes the origin of rich transverse responses of the conjugate physical quantities [31,32] such as the spin current generation [32,33], antisymmetric thermopolarization [34], nonlinear transverse magnetization [35], unconventional Hall effect [36], and nonlinear magnetostriction [37]. Meanwhile, magnetic instability under the ferroaxial ordering has not been fully clarified in spite of the Kramers degeneracy owing to the $\mathcal{T}$ symmetry. Thus, it is desirable to examine what types of magnetic instabilities occur under the ferroaxial ordering. Especially, it is important to understand how magnetic anisotropy is generated by the onset of the ferroaxial ordering, which might be helpful for understanding and exploring magnetic phase transitions in ferroaxial materials.

For that purpose, we analyze a typical d-orbital model with the d^1 configuration based on the multipole representation [38–46], where four types of multipoles with distinct $\mathcal{P}$ and $\mathcal{T}$ parities, electric, magnetic, magnetic toroidal, and electric toroidal, constitute a complete basis set in the low-energy Hilbert space [38,43,44]. Since the dipole component of the electric toroidal multipoles, i.e., the electric toroidal dipole (ETD), corresponds to the ferroaxial moment, we examine the magnetic instability in the presence of the ETD from the microscopic point of view beyond the symmetry. First, we perform perturbation and mean-field calculations for the single-sublattice d-orbital model. As a result, we show that the synergy between the molecular field arising from the ETD moment and the SOC leads to single-ion magnetic anisotropy, which tends to tilt the in-plane spin moments from the crystal axis.

Then, we analyze the d-orbital model in a four-site cluster. We find that the stability tendency of a vortex spin state accompanying both magnetic monopole and magnetic toroidal dipole is enhanced by the magnetic anisotropy characteristic of the ferroaxial moment. We show that the ratio of magnetic monopole and magnetic toroidal dipole becomes comparable to each other when the magnitude of the SOC is comparable

to that of the ETD molecular field. Our results indicate that the magnetic anisotropy arising from the ferroaxial moment can be a source of intriguing magnetic phases, which might exhibit a variety of cross-correlation phenomena.

The remaining part of this paper is organized as follows: In Sec. II C, we briefly introduce the ferroaxial moments based on the multipole representation. Then, we present a single-sublattice d-orbital model, and we show the role of the ferroaxial moment on the magnetic anisotropy through the second-order perturbative analysis. We also numerically evaluate the magnetic anisotropy by performing the mean-field calculations. Then, we show the stable magnetic textures under ETD moments in a four-site tetragonal cluster within the mean-field approximation in Sec. III. We show that the SOC under the ETD moment leads to a spin vortex phase accompanying both the magnetic monopole and magnetic toroidal dipole. Lastly, we summarize the results in Sec. IV. In Appendix A, we show the CEF dependence of the magnetic anisotropy. In Appendix B, we show the finite-temperature phase diagram when the exchange interaction for the ETD is considered. In Appendix C, we briefly show the result under the electric hexadecapole moment, which is another candidate hosting the ferroaxial moment in some crystals.

II. MAGNETIC ANISOTROPY UNDER FERROAXIAL MOMENT

We discuss the role of the ETD moment on magnetic anisotropy beyond the symmetry argument. In Sec. II A, we introduce the ETD moment, which corresponds to a ferroaxial moment. We also show when the ETD degree of freedom is activated in the Hilbert space. In Sec. II B, we introduce a single-sublattice five d-orbital model. Then, we perform the second-order perturbation theory by focusing on the role of the ETD moment in Sec. II C. Finally, we show the magnetic anisotropy within the mean-field calculations in Sec. II D.

A. Microscopic description of ferroaxial moment

The ferroaxial moment can appear when the mirror symmetry parallel to the moment direction is lost; the symmetry breakings in terms of $\mathcal{P}$ and $\mathcal{T}$ are not necessary. It is microscopically characterized by a ferroic alignment of a $\mathcal{T}$-even axial vector, which is referred to as the ETD $\boldsymbol{G}$. Based on the multipole description [43,44], the atomic-scale $\boldsymbol{G}$ operator is represented as the outer product of the spin operator $\boldsymbol{s} = \boldsymbol{\sigma}/2$ and orbital angular momentum operator $\boldsymbol{l}$ as follows:

$$\boldsymbol{G} = \boldsymbol{l} \times \boldsymbol{\sigma}, \tag{1}$$

where the schematic picture of $\boldsymbol{G}$ is shown in Fig. 1(a). It is noted that $\boldsymbol{G}$ can appear when the expectation values of $\boldsymbol{l}$ and $\boldsymbol{\sigma}$ are zero. Since both $\boldsymbol{l}$ and $\boldsymbol{\sigma}$ are axial vectors, the mirror symmetry parallel to $\boldsymbol{G}$ is broken, as shown in Fig. 1(b). Therefore, $\boldsymbol{G}$ can be activated in subspace with nonzero orbital angular moment, such as the p, d, and f orbitals. It is noted that the quantity $\boldsymbol{r} \times \boldsymbol{P}$, where $\boldsymbol{r}$ and $\boldsymbol{P}$ represent the position vector and the electric polarization, respectively, identically vanishes in an atomic wave function, although such a quantity has often been used to describe the ferroaxial moment in materials.

Among them, we consider five d orbitals in the low-energy Hilbert space in the following analysis. In this situation, $\boldsymbol{G}$ is

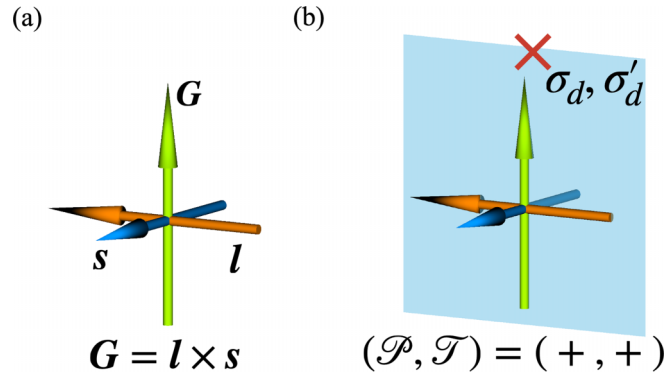

FIG. 1. (a) The representation of the atomic-scale ETD moment $\boldsymbol{G} = \boldsymbol{l} \times \boldsymbol{\sigma}$, which is denoted by the green arrow. The orange (blue) arrow represents the orbital (spin) angular momentum $\boldsymbol{l}(\boldsymbol{\sigma})$. (b) The symmetry of the atomic ETD moment; the mirror symmetry parallel to the ETD moment σ_v is lost. Meanwhile, time-reversal ($\mathcal{T}$) and spatial inversion ($\mathcal{P}$) symmetries are retained.

defined in the off-diagonal space between two orbitals with different total angular momenta $J = 3/2$ and $J = 5/2$.

B. Single-sublattice d-orbital model

In order to investigate the role of the ETD moment on the magnetic anisotropy, we introduce a single-sublattice five d-orbital model with $(d_u, d_v, d_{yz}, d_{zx}, d_{xy})$ for $u = 3z^2 - r^2$ and $v = x^2 - y^2$ on a simple square lattice. In the following analysis, we suppose the d^1 configuration and neglect the intra-atomic Coulomb interactions, with the transition metal magnetic ions in mind. The model Hamiltonian is given by

$$\mathcal{H} = \mathcal{H}^{\rm loc} + \mathcal{H}^{\rm ex}, \tag{2}$$

$$\mathcal{H}^{\rm loc} = \mathcal{H}^{\rm CEF} + \lambda \boldsymbol{l} \cdot \boldsymbol{s} - h_G G_z, \tag{3}$$

$$\mathcal{H}^{\rm ex} = -J_0\left(s_x^2 + s_y^2\right), \tag{4}$$

where the first term in Eq. (2) represents the one-body Hamiltonian, while the second term represents the two-body Hamiltonian. In $\mathcal{H}^{\rm loc}$, $\mathcal{H}_{\rm CEF}$ is the crystalline electric filed (CEF) Hamiltonian. We consider the five CEF parameters by supposing the D_{2h} symmetry: $\Delta_1 = 0.400$, $\Delta_2 \simeq 1.448$, $\Delta_3 = 2.200$, $\Delta_4 \simeq 2.552$, $\alpha \simeq 0.572$, and $\beta = \sqrt{1-\alpha^2}$, as schematically shown in Fig. 2(a); Δ_1–Δ_4 denote the atomic energy levels for d_{xy}, $-\alpha d_u + \beta d_v$, d_{zx}, and $\beta d_u + \alpha d_v$ orbitals measured from that for the d_{yz} orbital, where α and β stand for the numerical coefficients; see Appendix A for the detailed definition of $\mathcal{H}^{\rm CEF}$. We suppose that the ground-state energy level is the d_{yz} orbital. We also consider other CEF parameters, which is shown in Appendix D. We take the principal axis along the z direction, as shown in Fig. 2(b). The second term in Eq. (3) represents the atomic SOC. The third term in Eq. (3) represents the molecular field that arises from the ETD moment, which lowers the symmetry from D_{2h} to C_{2h}. One of the microscopic origins is the coupling to the rotational distortion of the lattice structure belonging to the same irreducible representation. Although we phenomenologically deal with such a molecular field, it is possible to evaluate h_G from the *ab initio* calculations. $\mathcal{H}^{\rm ex}$ in Eq. (4) represents the ferromagnetic exchange interaction within the

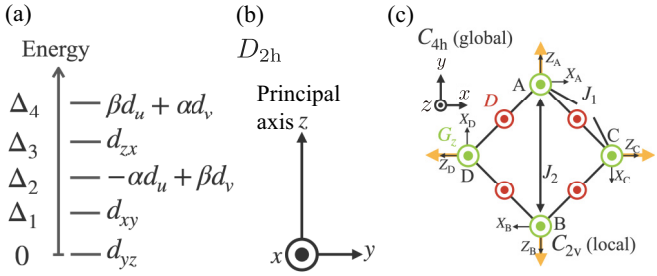

FIG. 2. (a) A schematic picture of the CEF levels for the single-sublattice five d-orbital model under the D_{2h} symmetry. (b) The coordinate axes for the single site, where the z axis is taken as the principal axis. (c) Four-site tetragonal cluster under the C_{4h} symmetry, where the site symmetry is C_{2v}. The global coordinate (x, y, z) and the local coordinate for sublattice i (X_i, Y_i, Z_i) are also shown. J_1 and J_2 represent the exchange interactions between the nearest-neighbor and next-nearest-neighbor sites, respectively. Yellow arrows represent the electric polarization $\boldsymbol{P}$, which originates from the potential gradient at each site. Green (red) circles represent ETD moments (DM vectors) along the z direction.

single-sublattice unit cell. We ignore other multipole interactions in order to focus on the magnetic instability under the ferroaxial moment.

C. Perturbation analysis

We examine the magnetic anisotropy arising from the ETD moment by performing the perturbation analysis. For that purpose, we analyze $\mathcal{H}^{\rm loc}$ in Eq. (3) by ignoring $\mathcal{H}^{\rm ex}$ in Eq. (4). Within the second-order perturbation in terms of λ and h_G, an effective spin Hamiltonian is derived as

$$\mathcal{H}_{\rm s} = -\sum_{\mu,\nu=x,y} \Lambda_{\mu\nu} s_\mu s_\nu, \tag{5}$$

$$\boldsymbol{\Lambda} = \begin{bmatrix} 4h_G^2\Lambda'_{yy} + \lambda^2\Lambda'_{xx} & -2h_G\lambda(\Lambda'_{xx} - \Lambda'_{yy}) \\ -2h_G\lambda(\Lambda'_{xx} - \Lambda'_{yy}) & 4h_G^2\Lambda'_{xx} + \lambda^2\Lambda'_{yy} \end{bmatrix}, \tag{6}$$

where

$$\Lambda'_{\mu\nu} = \sum_e \frac{\langle g|l_\mu|e\rangle\langle e|l_\nu|g\rangle}{E_e - E_g}. \tag{7}$$

$\Lambda'_{\mu\nu}$ includes the contribution from the CEF, where $|g\rangle$ ($|e\rangle$) is the ground state (excited state) and $E_g(E_e)$ is the ground-state (excited-state) energy. We here omit the z component of $\Lambda_{\mu\nu}$, since the effect of the ETD does not appear in $\Lambda_{z\nu}$ and $\Lambda_{\mu z}$.

There are three important observations in Eq. (6). One is the emergence of the off-diagonal xy component in $\Lambda_{\mu\nu}$. Thus, the ferroaxial moment induced by h_G tends to tilt the spin moment from the crystal axis. In addition, it is noteworthy that the SOC λ is necessary to induce the off-diagonal component. The second is the importance of the low-symmetric CEF to induce Λ_{xy}, since it is proportional to $\Lambda'_{xx} - \Lambda'_{yy}$ for $\Lambda'_{xx} \neq \Lambda'_{yy}$. In other words, the inequivalence between the x and y directions is significant. This is why we consider the orthorhombic CEF Hamiltonian under the D_{2h} symmetry in $\mathcal{H}^{\rm CEF}$; $\Lambda_{xy} = 0$ when the tetragonal and hexagonal CEFs are considered. The last is the opposite tendency in the diagonal component of $\Lambda_{\mu\nu}$ for $\mu = \nu$ between the ETD moment and the SOC; h_G (λ) tends to favor the x (y) direction for $\Lambda'_{xx} < \Lambda'_{yy}$. The qualitative tendencies for the above observations remain robust even when quantum and thermal fluctuations are introduced.

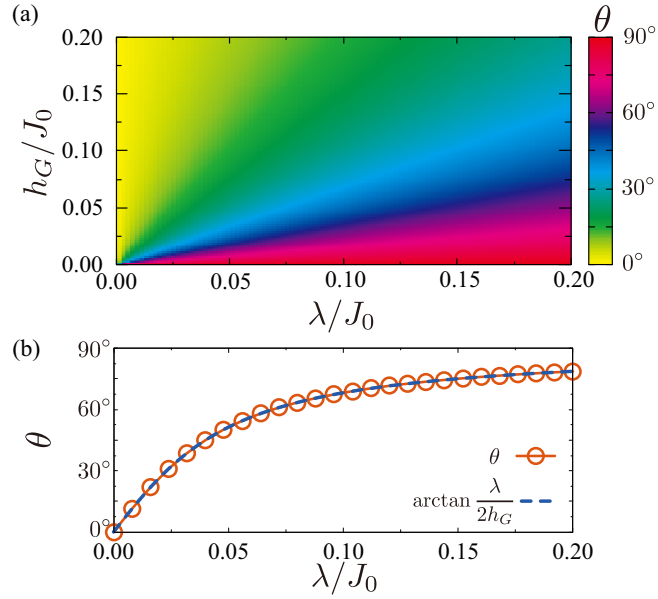

FIG. 3. (a) Contour plot of the tilt angle of a spin moment θ in the plane of λ and h_G, which is obtained by the mean-field calculations. (b) λ dependence of the numerical result (red circle) and the perturbation result (blue-dashed line) at $h_G = 0.02$. In both panels, the data is calculated by changing λ and/or h_G with the interval of $\Delta_\lambda/J_0 = \Delta_{h_G}/J_0 = 0.002$.

More specifically, one obtains the tilt angle θ from the x axis by diagonalizing $\boldsymbol{\Lambda}$, which is given by $\theta = \arctan[\lambda/(2h_G)]$ for $\Lambda'_{xx} < \Lambda'_{yy}$ or $\arctan(-2h_G/\lambda)$ for $\Lambda'_{xx} > \Lambda'_{yy}$. In the case of the CEF parameters in Fig. 2(a), $\Lambda'_{xx} < \Lambda'_{yy}$. We discuss the magnetic anisotropy for the other CEF levels in Appendix A.

D. Mean-field calculations

We numerically evaluate the tilt angle θ in the presence of the two-body Hamiltonian $\mathcal{H}^{\rm ex}$. In order to capture the essence, we apply the mean-field approximation for $\mathcal{H}^{\rm ex}$ as

$$\mathcal{H}^{\rm ex}_{\rm MF} = -J_0(\langle s_x\rangle s_x + \langle s_y\rangle s_y) + ({\rm const.}), \tag{8}$$

where $\langle\cdots\rangle$ represents the statistical average in d^1 configuration. We ignore the effect of quantum and thermal fluctuations beyond the mean-field approximation for simplicity, which can be a source of nontrivial states such as valence-bond solid states [47]. We set J_0 to the energy unit of the single-sublattice model ($J_0 = 1$).

Figure 3(a) shows the angle θ of the spin moment measured from the x axis by changing λ and h_G at temperature $T/J_0 = 0.1$. When either λ or h_G becomes zero, the spin aligns in the crystal axis. For $\lambda/J_0 = 0$, the spin moment aligns in the x direction, while it aligns in the y direction for $h_G/J_0 = 0$. This feature is consistent with the perturbation analysis, where $\Lambda'_{xx} < \Lambda'_{yy}$ is satisfied.

Meanwhile, the spin tilts from the crystal axis when both λ and h_G are considered. One finds good agreement between

numerical and perturbation results; see the λ dependence of both results in the case of $h_G/J_0 = 0.02$ in Fig. 3(b). In addition, the maximum tilt angle of $\theta = 45^\circ$ is realized for $\lambda \simeq 2h_G$, which is also consistent with the perturbation result in Eq. (6); the feature holds when λ increases. These results indicate that the interplay between λ and h_G plays an important role in inducing the magnetic anisotropy characteristic of the ETD moment even beyond the perturbation regime.

III. MAGNETIC INSTABILITY IN A CLUSTER MODEL

A. Four-site cluster model

Next, let us consider the magnetic instability under the ETD moment in a cluster system by extending the analysis from the single-sublattice system. We consider a four-site tetragonal cluster under the C_{4h} symmetry, as shown in Fig. 2(c). We suppose that the site symmetry is C_{2v} so that the off-diagonal component in $\Lambda_{\mu\nu}$ in Eq. (6) becomes nonzero. We use the local Hamiltonian $\mathcal{H}^{\rm loc}$ in Sec. II B by adding the sublattice index $i =$ A–D. We take the same CEF parameters in Sec. II C, although α take opposite sign and $d_{yz} \leftrightarrow d_{zx}$ between (A, B) and (C, D) sublattices because the principal axis for the A and B sublattices is different from that for the C and D sublattices by 90°.

For the exchange interaction, we consider the following Hamiltonian, which is given by

$$\mathcal{H}'^{\rm ex} = -J_1 \sum_{\langle i,j\rangle}^{\rm n.n} \left(s_x^i s_x^j + s_y^i s_y^j\right) - J_2 \sum_{\langle i,j\rangle}^{\rm n.n.n} \left(s_x^i s_x^j + s_y^i s_y^j\right), \quad (9)$$

where J_1 and J_2 correspond to the coupling constants for the nearest-neighbor (n.n.) and next-nearest-neighbor (n.n.n) sites, respectively. We here consider the situation where magnetic ordering with the in-plane spin modulations occurs rather than the out-of-plane ones. In addition, we consider the DM interaction $\boldsymbol{D} = (D_x, D_y, D_z)$. From the symmetry viewpoint, only the z component between the nearest-neighbor sites becomes finite, as shown in Fig. 2(c). The DM Hamiltonian is given by

$$\mathcal{H}^{\rm DM} = -\sum_{\langle i,j\rangle}^{\rm n.n} D_z^{ij} (\boldsymbol{s}^i \times \boldsymbol{s}^j)_z, \quad (10)$$

where $D_z^{\rm AD} = -D_z^{\rm DA} = D_z^{\rm DB} = -D_z^{\rm BD} = D_z^{\rm BC} = -D_z^{\rm CB} = D_z^{\rm CA} = -D_z^{\rm AC} \equiv D$. It is noted that we phenomenologically introduce the DM interaction from the symmetry while keeping the SOC term in $\mathcal{H}^{\rm loc}$; the double counting of the SOC for the DM interaction and $\mathcal{H}^{\rm loc}$ does not affect the following qualitative results. By adopting the mean-field approximation, $\mathcal{H}'^{\rm ex}$ and $\mathcal{H}^{\rm DM}$ are represented as

$$\mathcal{H}'^{\rm ex}_{\rm MF} \simeq -J_1 \sum_{i}^{\rm A,B,C,D} \sum_{j}^{\rm n.n} \left(\langle s_x^i\rangle s_x^j + \langle s_y^i\rangle s_y^j\right) - J_2 \sum_{i}^{\rm A,B,C,D} \sum_{j}^{\rm n.n.n} \left(\langle s_x^i\rangle s_x^j + \langle s_y^i\rangle s_y^j\right), \quad (11)$$

$$\mathcal{H}^{\rm DM}_{\rm MF} \simeq -\sum_{i}^{\rm A,B,C,D} \sum_{j}^{\rm n.n} D_z^{ij} [\langle \boldsymbol{s}^i\rangle \times \boldsymbol{s}^j]_z, \quad (12)$$

where we omit the constant term for notational simplicity. We set J_1 to the energy unit of the four-site cluster model ($J_1 = 1$). Although we treat the effect of the ETD as the one-body mean field h_G for simplicity, a qualitatively similar result can be obtained even when the ETD moment is induced through the two-body exchange interaction, as discussed in Appendix B.

B. Spin configurations

We consider the magnetic instability in the four-site cluster model within the mean-field approximation. Since we suppose the in-plane magnetic anisotropy, the four-sublattice magnetic structures are expressed as a linear combination of eight independent spin configurations. Based on the cluster multipole theory [48], they are classified into magnetic and magnetic toroidal multipoles: magnetic monopole ($M_0^{(c)}$), magnetic dipole ($M_x^{(c)}, M_y^{(c)}$), magnetic toroidal dipole ($T_z^{(c)}$), magnetic quadrupole ($M_{xy}^{(c)}, M_v^{(c)}$), and magnetic toroidal quadrupole ($T_{yz}^{(c)}, T_{zx}^{(c)}$). Specifically, their spin configurations denoted as ($\sigma_x^{\rm A}, \sigma_y^{\rm A}, \sigma_x^{\rm B}, \sigma_y^{\rm B}, \sigma_x^{\rm C}, \sigma_y^{\rm C}, \sigma_x^{\rm D}, \sigma_y^{\rm D}$) are given by

$$M_0^{(c)} = (0, 1, 0, -1, 1, 0, -1, 0), \quad (13)$$

$$M_x^{(c)} = (1, 0, 1, 0, 1, 0, 1, 0), \quad (14)$$

$$M_y^{(c)} = (0, 1, 0, 1, 0, 1, 0, 1), \quad (15)$$

$$T_z^{(c)} = (1, 0, -1, 0, 0, -1, 0, 1), \quad (16)$$

$$M_{xy}^{(c)} = (1, 0, -1, 0, 0, 1, 0, -1), \quad (17)$$

$$M_v^{(c)} = (0, -1, 0, 1, 1, 0, -1, 0), \quad (18)$$

$$T_{yz}^{(c)} = (1, 0, 1, 0, -1, 0, -1, 0), \quad (19)$$

$$T_{zx}^{(c)} = (0, 1, 0, 1, 0, -1, 0, -1). \quad (20)$$

The lowest-energy spin configuration depends on the magnetic interactions (J_1, J_2, D) as well as $\mathcal{H}^{\rm loc}$. When $D/J_1 = 0$, $|J_1| < |J_2|$, $J_2 < 0$, and $\mathcal{H}^{\rm loc}$ is negligible, the energy by the exchange interactions becomes the lowest for any of $M_0^{(c)}, T_z^{(c)}, M_v^{(c)}$, and $M_{xy}^{(c)}$. In this situation, by introducing $D > 0$, the energy for $M_0^{(c)}$ and $T_z^{(c)}$ is smaller than that for $M_v^{(c)}$ and $M_{xy}^{(c)}$. With this tendency in mind, we take $|J_1| \sim |J_2|$, $J_2 < 0$, and $D/J_1 = 0.05 > 0$. Although the energy for $M_0^{(c)}$ and $T_z^{(c)}$ is degenerate with each other, it splits by taking into account the effect of the $\mathcal{H}^{\rm loc}$.

C. Magnetic phase diagram

We perform the self-consistent mean-field calculations for the four-site cluster model by setting $h_G/J_1 = 0.2$ and the temperature as $T/J_1 = 0.1$. Figure 5(a) shows the magnetic phase diagram by changing λ and J_2. There are mainly two phases in the phase diagram: Phase I and Phase II.

The spin configuration of Phase I is expressed as the linear combination of $M_x^{(c)}, M_y^{(c)}, T_{yz}^{(c)}$, and $T_{zx}^{(c)}$; the spin moments tilt from the crystal axis owing to the magnetic anisotropy arising from h_G. Although Phase I is almost characterized by the ferromagnetic spin configuration, i.e., $M_x^{(c)}$ and $M_y^{(c)}$, it includes the small contribution from $T_{yz}^{(c)}$ and $T_{zx}^{(c)}$. This is

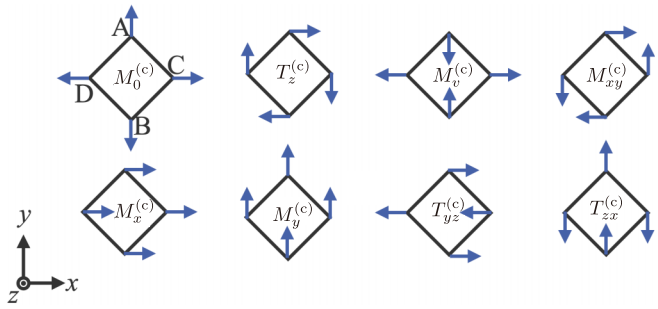

FIG. 4. Eight independent spin configurations in the four-site cluster: magnetic monopole ($M_0^{(c)}$), magnetic dipole ($M_x^{(c)}, M_y^{(c)}$), magnetic toroidal dipole ($T_z^{(c)}$), magnetic quadrupole ($M_{xy}^{(c)}, M_v^{(c)}$), and magnetic toroidal quadrupole ($T_{yz}^{(c)}, T_{zx}^{(c)}$). Blue arrows represent the spin moments at each site.

because the C_2 axis for the A and B sublattices in the local coordinate [yellow arrows in Fig. 2(c)] is different from that for the C and D sublattices by 90°, which means that x and y axes in the global coordinate are inequivalent for the (A, B) and (C, D) sublattices, and hence, the spin lengths between them are different from each other when the in-plane moments are parallel/antiparallel to each other.

Meanwhile, Phase II is characterized by the spin configuration to possess the fourfold rotational symmetry in order to gain the energy by the CEF. For $J_2/J_1 < -0.9$ and $\lambda/J_1 = 0$, the spin configuration in Phase II corresponds to $T_z^{(c)}$. By introducing λ, the spins at four sublattices tilt in the same manner so as to keep the fourfold rotational symmetry, which indicates that the spin configuration is expressed as the linear combination of $M_0^{(c)}$ and $T_z^{(c)}$, as schematically shown in the inset of Fig. 5(a).

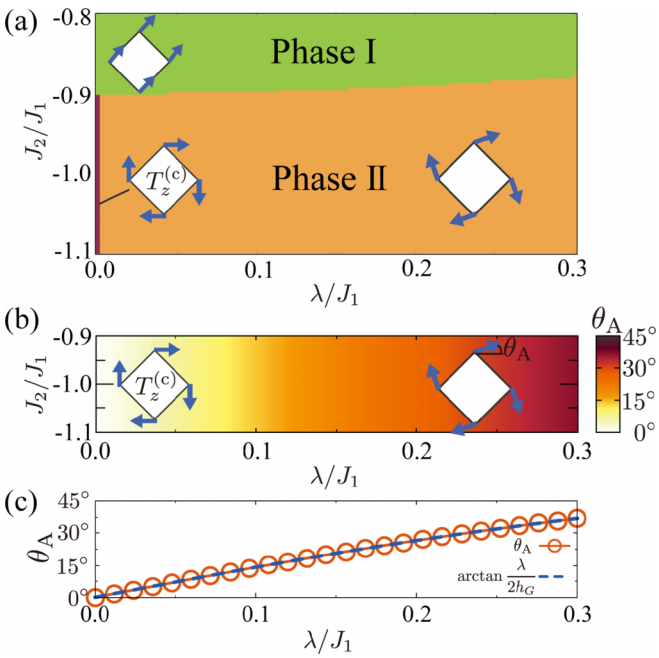

FIG. 5. (a) λ–J_2 phase diagram obtained at $h_G/J_1 = 0.2$ and $D/J_1 = 0.05$. The data is calculated by changing λ and h_G with the interval of $\Delta_\lambda/J_1 = \Delta_{J_2}/J_1 = 0.003$. Phase I (II) represents the spin configuration consisting of the linear combination of $M_x^{(c)}$, $M_y^{(c)}$, $T_{yz}^{(c)}$, and $T_{zx}^{(c)}$ ($M_0^{(c)}$ and $T_z^{(c)}$) in Fig. 4. At $\lambda/J_1 = 0$ for $J_2/J_1 < -0.9$, the $T_z^{(c)}$ state is stabilized. (b) Contour plot of the tilt angle of spin moments at A sublattice θ_A for $-1.1 \leqslant J_2/J_1 \leqslant -0.9$. (c) λ dependence of the numerical result (red circle) and the perturbation result (blue dashed line) in terms of θ_A at $J_2/J_1 = -1.1$.

We discuss the effect of $\mathcal{H}^{\rm loc}$ including the ETD molecular field h_G and the SOC λ for $J_2/J_1 < -0.9$. In the case of $\mathcal{H}^{\rm loc} = 0$, the phase boundary between Phase I and Phase II is given by $J_2/J_1 = -0.95$. Thus, $\mathcal{H}^{\rm loc}$ tends to favor the region for Phase II. This is understood from the fact that $\mathcal{H}^{\rm loc}$, which becomes the origin of the magnetic anisotropy, favors the spin configuration satisfying the fourfold rotational symmetry that the four-site cluster possesses in order to gain the energy by the magnetic anisotropy. Such a tendency holds for nonzero λ, which enhances the magnetic anisotropy; the phase boundary moves upward by increasing λ. Thus, both h_G and λ tend to favor the vortex spin configuration retaining the fourfold rotational symmetry compared to the uniform one breaking the fourfold rotational symmetry.

Figure 5(b) shows the tilt angle of spin moments at A sublattice θ_A in Phase II for $-1.1 \leqslant J_2/J_1 \leqslant -0.9$. The behavior is similar to that in the single-sublattice model; the tilt angle increases as λ increases. Furthermore, we confirmed that such behavior is understood from the perturbation calculations, as shown in Fig. 5(c); both data are well consistent.

Finally, we discuss the relationship between the ETD moment and vortex magnetic structures from the symmetry viewpoint. Since M_0 corresponds to a time-reversal-odd axial scalar and T_z corresponds to a time-reversal-odd polar vector, their product $M_0 T_z$ corresponds to a time-reversal-even axial vector, i.e., the ETD G_z [49]. In this sense, the appearance of Phase II, which is expressed as the linear combination of M_0 and T_z in the presence of G_z, is natural. In a similar context, it was shown that the skyrmion crystal accompanying both M_0 (Néel type) and T_z (Bloch type) is realized by considering the magnetic anisotropy that originates from the mirror symmetry breaking [50]. Since M_0 and T_z lead to similar but different physical phenomena, the coexisting state can give rise to further intriguing cross-correlation responses and transports. The electric axial moment G_z plays an important role in inducing such an effective coupling of M_0 and T_z.

IV. SUMMARY

To summarize, we have investigated the magnetic single-ion anisotropy and its associated magnetic instability driven by the ETD moments based on the perturbation and mean-field calculations for the five d-orbital models in the single-sublattice system and four-site cluster system. We show that the synergy between the molecular field arising from the ETD moment and the SOC is essential to induce the in-plane magnetic anisotropy so that the spin tilts from the crystal axis beyond the symmetry viewpoint. We also show that the tendency to tilt the spin moments is enhanced when the ETD molecular field and SOC are comparable to each other. We discuss that the ferroaxial system might become a prototype to realize the vortex spin texture with both the nature of the

magnetic monopole and magnetic toroidal dipole in collaboration with the exchange interactions.

The present tendency in terms of magnetic anisotropy is also expected for other ferroaxial materials. Since the ferroaxial moment can appear in crystallographic point groups without mirror symmetry parallel to the electric axial moment, C_{6h}, C_6, C_{3h}, C_{4h}, C_4, S_4, C_{3i}, C_3, C_{2h}, C_2, C_s, C_i, and C_1, the materials with these crystal structures can exhibit similar vortex spin configurations when the magnetic phase transition occurs.

Let us comment on the difference between the ETD and other multipole degrees of freedom, which might also correspond to the electric axial moments in some crystals. Although the ETD and other multipoles are independent of each other in the rotational group, they often belong to the same irreducible representation according to the symmetry lowering. In the cases of the C_{2h} and C_{4h} symmetries discussed in Secs. II C and III, respectively, the $xy(x^2-y^2)$ type of the electric hexadecapole also leads to similar mirror symmetry breaking. Thus, the electric hexadecapole is another candidate to describe the ferroaxial ordering. Indeed, we find that the electric hexadecapole also leads to the tilt of spin moments, although its behavior against the model parameters is different. We discuss the difference between the ETD and electric hexadecapole in Appendix C.

ACKNOWLEDGMENTS

This research was supported by JSPS KAKENHI Grants No. JP21H01037, No. JP22H04468, No. JP22H00101, JP22H01183, No. JP23K03288, No. JP23H04869, and by JST PRESTO (JPMJPR20L8) and JST CREST (JPMJCR23O4).

APPENDIX A: CEF DEPENDENCE OF MAGNETIC ANISOTROPY

In this Appendix, we show the relation between CEF parameters and the magnetic anisotropy. As shown in Eq. (7), the CEF energy levels and the matrix elements of orbital angular momentum l_x, l_y affect the magnitude of anisotropy Λ'_{xx}, Λ'_{yy}. The matrix elements of l_x and l_y are given by

$$l_x = \begin{pmatrix} 0 & 0 & i\sqrt{3} & 0 & 0 \\ 0 & 0 & i & 0 & 0 \\ -i\sqrt{3} & -i & 0 & 0 & 0 \\ 0 & 0 & 0 & 0 & i \\ 0 & 0 & 0 & -i & 0 \end{pmatrix}, \tag{A1}$$

$$l_y = \begin{pmatrix} 0 & 0 & 0 & -i\sqrt{3} & 0 \\ 0 & 0 & 0 & i & 0 \\ 0 & 0 & 0 & 0 & -i \\ i\sqrt{3} & -i & 0 & 0 & 0 \\ 0 & 0 & i & 0 & 0 \end{pmatrix}, \tag{A2}$$

where the basis is given by five d orbitals: $|d_u\rangle$, $|d_v\rangle$, $|d_{yz}\rangle$, $|d_{zx}\rangle$, $|d_{xy}\rangle$. $l_x(l_y)$ has the matrix elements between d_u and d_{yz}, d_v and d_{yz}, and d_{zx} and d_{xy} (d_u and d_{zx}, d_v and d_{zx}, and d_{yz} and d_{xy}). To investigate the relation between CEF levels and magnetic anisotropy, we rewrite the local CEF Hamiltonian as

$$\mathcal{H}^{\rm loc} = \sum_k^5 B_k O_k, \tag{A3}$$

where

$$O_1 = \frac{1}{\sqrt{2}}\begin{pmatrix} 1 & 0 & 0 & 0 & 0 \\ 0 & -1 & 0 & 0 & 0 \\ 0 & 0 & 0 & 0 & 0 \\ 0 & 0 & 0 & 0 & 0 \\ 0 & 0 & 0 & 0 & 0 \end{pmatrix}, \quad O_2 = \frac{1}{\sqrt{2}}\begin{pmatrix} 0 & 1 & 0 & 0 & 0 \\ 1 & 0 & 0 & 0 & 0 \\ 0 & 0 & 0 & 0 & 0 \\ 0 & 0 & 0 & 0 & 0 \\ 0 & 0 & 0 & 0 & 0 \end{pmatrix},$$

$$O_3 = \begin{pmatrix} 0 & 0 & 0 & 0 & 0 \\ 0 & 0 & 0 & 0 & 0 \\ 0 & 0 & 1 & 0 & 0 \\ 0 & 0 & 0 & 0 & 0 \\ 0 & 0 & 0 & 0 & 0 \end{pmatrix}, \quad O_4 = \begin{pmatrix} 0 & 0 & 0 & 0 & 0 \\ 0 & 0 & 0 & 0 & 0 \\ 0 & 0 & 0 & 0 & 0 \\ 0 & 0 & 0 & 1 & 0 \\ 0 & 0 & 0 & 0 & 0 \end{pmatrix}, \quad O_5 = \begin{pmatrix} 0 & 0 & 0 & 0 & 0 \\ 0 & 0 & 0 & 0 & 0 \\ 0 & 0 & 0 & 0 & 0 \\ 0 & 0 & 0 & 0 & 0 \\ 0 & 0 & 0 & 0 & 1 \end{pmatrix}. \tag{A4}$$

We take the principal axis as the y direction by supposing the cartesian coordinate for the A sublattice in Fig. 2(c). B_1, B_3, B_4, and B_5 represent the parameters for the atomic-energy level, while B_2 represents the parameter for the hybridization between the d_u and d_v orbitals.

Figures 6(a), 6(c), and 6(e) [6(b), 6(d), and 6(f)] represent the B_2 dependencies of CEF energy levels (Λ'_{xx}, Λ'_{yy} and $\Lambda'_{xx}-\Lambda'_{yy}$) by setting $B_1 = 0.5$, $B_3 = -2.0$, and $B_5 = 0.2$. We set $B_4 = -2.5$ for Figs. 6(a) and 6(b), $B_4 = -1.6$ for Figs. 6(c) and 6(d), and $B_4 = -1.3$ for Figs. 6(e) and 6(f).

In the case of Figs. 6(a) and 6(b), the ground state is occupied by the d_{xy} orbital, which leads to nonzero matrix elements $\langle e|\, l_x\, |g\rangle$ ($\langle e|\, l_y\, |g\rangle$) for $\langle e| = \langle d_{zx}|$ ($\langle d_{yz}|$). Thus, B_2 does not affect both Λ'_{xx} and Λ'_{yy}.

On the other hand, when the ground state is occupied by the d_{yz} orbital, the anisotropy depends on B_2, as shown in Figs. 6(c)–6(f), since $\langle e|\, l_x\, |g\rangle$ ($\langle e|\, l_y\, |g\rangle$) becomes nonzero for $\langle e| = \langle d_u|$, $\langle d_v|$ ($\langle d_{xy}|$). In such a situation, energy levels of $-\alpha d_u + \beta d_v (\beta d_u + \alpha d_v)$ and the ratio of d_u in the lower eigenstate affect Λ'_{xx}. When B_2 becomes larger, $|\alpha|$ becomes smaller as shown in the insets of Figs. 6(c) and 6(e), thereby Λ'_{xx} decreases because of $|\,\langle d_u|l_x|d_{yz}\rangle\,| > |\,\langle d_v|l_x|d_{yz}\rangle\,|$. On the other hand, Λ'_{yy} is independent of B_2 as the energy of d_{xy} is constant against B_2. Depending on the CEF parameters, the sign change of $\Lambda'_{xx}-\Lambda'_{yy}$ occurs, as shown in Fig. 6(f).

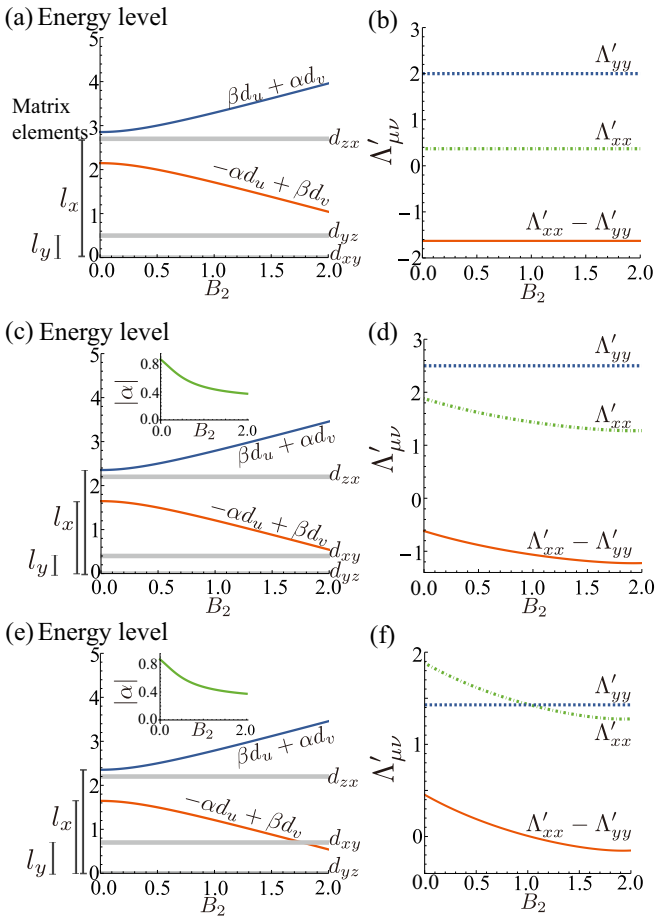

FIG. 6. B_2 dependence of (a), (c), (e) energy levels and (b), (d), (f) $\Lambda'_{\mu\nu}(\mu, \nu = x, y)$ at $B_4 = -2.5$ in (a), (b), $B_4 = -1.6$ in (c), (d), and $B_4 = -1.3$ in (e), (f) for the single-sublattice system. The red(blue) line represents the CEF energy level $-\alpha d_u + \beta d_v(\beta d_u + \alpha d_v)$. The insets of (c) and (e) show B_2 dependence of $|\alpha|$. The ground-state energy level is characterized by the d_{xy} (d_{yz}) orbital for (a) and (b) [(c), (d), (e), and (f)]. The other model parameters are chosen as $B_1 = 0.5$, $B_3 = -2$, and $B_5 = 0.2$.

APPENDIX B: FINITE-TEMPERATURE PHASE DIAGRAM IN THE PRESENCE OF THE EXCHANGE INTERACTION BETWEEN THE ELECTRIC TOROIDAL DIPOLES

In the main text, we deal with the effect of the ETD moment as the one-body molecular-field term h_G. In this Appendix, we introduce the two-body exchange interaction between the ETD moments instead of h_G, which is given by

$$\mathcal{H}^{\mathrm{G}} = -\sum_{\langle ij \rangle} J_G^{ij} G_z^i G_z^j, \tag{B1}$$

where J_G^{ij} is the coupling constant for the nearest-neighbor sites, i.e., $J_G^{ij} = J_G$. The microscopic origin of this interaction might be attributed to the multiorbital Coulomb interactions, such as the interorbital Coulomb interaction and pair-hopping interaction. We apply the mean-field approximation as

$$\mathcal{H}^{\mathrm{G}}_{\mathrm{MF}} = -J_G \sum_{i}^{\mathrm{A,B,C,D}} \sum_{j}^{\mathrm{n.n}} \langle G_z^i \rangle G_z^j + (\text{const.}). \tag{B2}$$

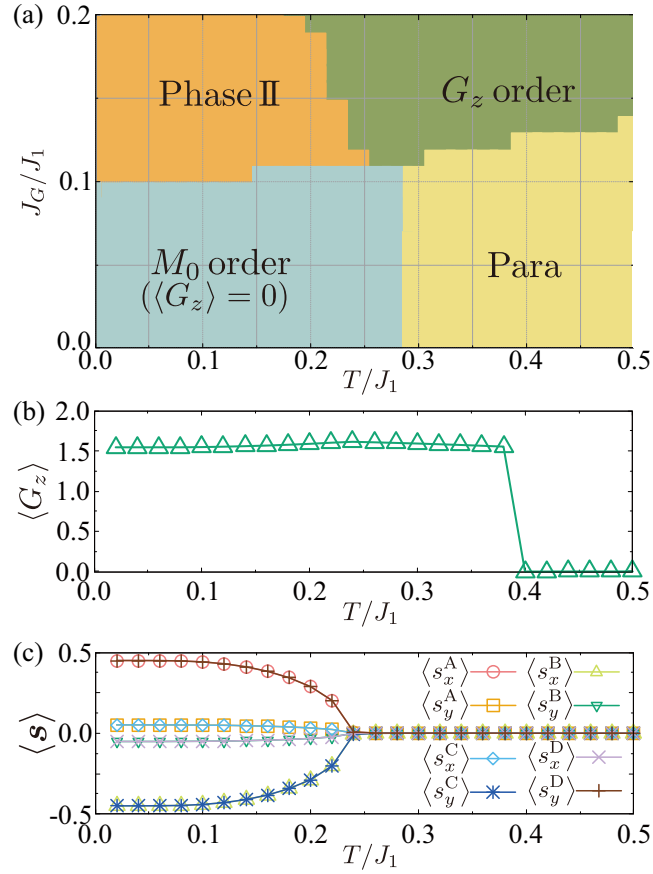

FIG. 7. (a) T–J_G phase diagram at $\lambda/J_1 = 0.1$. The T dependence of (b) $\langle G_z \rangle$ and (c) $\langle s_x^{\mathrm{A}} \rangle$, $\langle s_y^{\mathrm{A}} \rangle$, $\langle s_x^{\mathrm{B}} \rangle$, $\langle s_y^{\mathrm{B}} \rangle$, $\langle s_x^{\mathrm{C}} \rangle$, $\langle s_y^{\mathrm{C}} \rangle$, $\langle s_x^{\mathrm{D}} \rangle$, $\langle s_y^{\mathrm{D}} \rangle$ at $J_G/J_1 = 0.12$. The data is calculated by changing T and J_G with the interval of $\Delta T/J_1 = 0.02$, $\Delta J_G/J_1 = 0.01$. The other parameters are the same as those used in Fig. 5.

By performing the self-consistent calculations for the four-site cluster model $\sum_i \mathcal{H}_i^{\mathrm{loc}} + \mathcal{H}'^{\mathrm{ex}}_{\mathrm{MF}} + \mathcal{H}^{\mathrm{DM}}_{\mathrm{MF}} + \mathcal{H}^{\mathrm{G}}_{\mathrm{MF}}$, we obtain the finite-temperature phase diagram against J_G in Fig. 7. We choose the same model parameters as those in Sec. III except for $h_G = 0$.

Similarly to the results in Sec. III in the main text, one finds that a sequence of the phase transition occurs for $J_G/J_1 \gtrsim 0.1$; in the case of $J_G/J_1 = 0.12$, the paramagnetic state with $\langle G_z \rangle = 0$ turns into the ferroaxial state with $\langle G_z \rangle \neq 0$ at $T/J_1 \simeq 0.4$, and this state shows a further transition to Phase II at $T/J_1 \simeq 0.24$ by decreasing the temperature. Here, the spin configuration in Phase II is characterized by the linear combination of the magnetic monopole and magnetic toroidal dipole, as discussed in the main text. We show the behavior of $\langle G_z \rangle$ and spin moments $\langle s_\mu^i \rangle$ for $i =$ A–D and $\mu = x, y$ in Figs. 7(b) and 7(c), respectively. Thus, the phase transition from the ferroaxial state to the vortex spin state occurs in a unified way once the ferroaxial moment is induced.

APPENDIX C: RESULT FOR ELECTRIC HEXADECAPOLE

Although we have investigated the ferroaxial ordering under the ETD moment in the main text, other multipoles also lead to the ferroaxial ordering when their irreducible

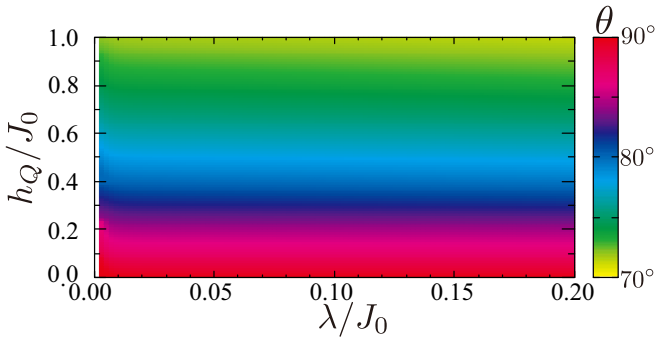

FIG. 8. Contour plot of the tilt angle θ of the spin moments under the Q^{α}_{4z} molecular field. The other parameters are the same as those used in Fig. 3. It is noted that θ is indeterminate for $\lambda/J_0 = 0$ owing to no magnetic anisotropy in the xy plane.

representations are the same as each other. In the d-orbital space, the electric hexadecapole $Q^{\alpha}_{4z}[\propto xy(x^2 - y^2)]$ is another degree of freedom related to the ferroaxial moments, since Q^{α}_{4z} belongs to the same irreducible representation as G_z under the D_{2h} symmetry. In this Appendix, we briefly discuss the result for the Q^{α}_{4z} ordered phase. We analyze the single-sublattice model, where we replace the mean-field term $-h_G G_z$ to $-h_Q Q^{\alpha}_{4z}$ in Eq. (3). The other model parameters are the same as those used in Sec. II C

Figure 8 shows the contour plot of the tilt angle θ by changing λ and h_Q, which is obtained by the self-consistent mean-field calculations. In contrast to the result in Fig. 3 in Sec. II C in the main text, θ does not depend on λ, while h_Q tilts the spin moments from the crystal axis. This behavior is attributed to the anisotropic form factor of $\Lambda'_{\mu\nu}$. In the presence of Q^{α}_{4z} without the spin component, the spin Hamiltonian in terms of the x and y spin components is represented as

$$\mathcal{H}'_{\rm s} = -\lambda^2 \sum_{\mu,\nu=x,y} \Lambda'_{\mu\nu} s_\mu s_\nu, \tag{C1}$$

where Λ'_{xx}, Λ'_{yy}, and Λ'_{xy} can become nonzero in the presence of h_Q in contrast to Λ_{xy} in Sec. II C.

By diagonalizing $\mathbf{\Lambda}'$ in Eq. (C1), one obtains θ as follows:

$$\theta = \arctan\left[\frac{2\Lambda'_{xy}}{\sqrt{(\Lambda'_{xx} - \Lambda'_{yy})^2 + 4\Lambda'^2_{xy}} + \Lambda'_{xx} - \Lambda'_{yy}}\right]. \tag{C2}$$

Thus, one finds that θ has no λ dependence, which is consistent with the numerical results in Fig. 8.

APPENDIX D: RESULT FOR DIFFERENT CEF PARAMETERS

In this Appendix, we show the result for a different choice of the CEF levels. We adopt the situation where the CEF levels for the d_{yz}, d_{zx}, and d_{xy} orbitals are apart from the d_u and d_v orbitals, as often found in transition-metal oxides; we set $\Delta_1 = 0.5$, $\Delta_2 = 1$, $\Delta_3 \simeq 2.13944$, $\Delta_4 \simeq 2.86056$, $\alpha \simeq 0.812542$, and $\beta = \sqrt{1-\alpha^2}$. The CEF levels are shown in Fig. 9(a).

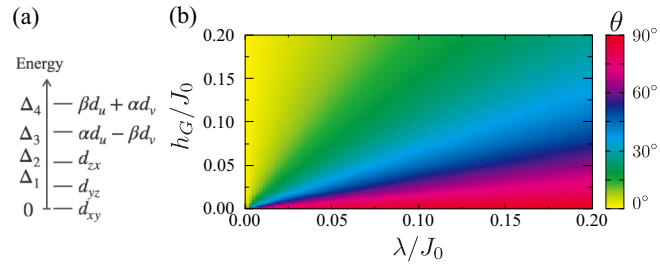

FIG. 9. (a) A schematic picture of the CEF levels for the single-sublattice five d-orbital model under the D_{2h} symmetry. (b) Contour plot of the tilt angle of a spin moment θ in the plane of λ and h_G, which is obtained by the mean-field calculations for $\Delta_1 = 0.5$, $\Delta_2 = 1$, $\Delta_3 \simeq 2.13944$, $\Delta_4 \simeq 2.86056$, $\alpha \simeq 0.812542$, and $\beta = \sqrt{1-\alpha^2}$.

Figure 9(b) shows the tilt angle of a spin moment θ for a single-sublattice model. Compared with the results in Fig. 3, one finds a similar tendency; the tilt angle becomes the maximum when the SOC λ is comparable to the ETD molecular field h_G. This result indicates that our qualitative argument in the main text holds irrespective of a sequence of the CEF levels.

APPENDIX E: THREE-SITE CLUSTER MODEL

In order to show that the magnetic behavior in a four-site cluster in Sec. III is expected to happen for other clusters, we consider the magnetic instability for a three-site triangle cluster model, as shown in Fig. 10(a). Similar to the procedure in Sec. III B, the independent six magnetic structures are classified into the cluster multipole orderings as follows: magnetic monopole ($M_0^{(c)}$), magnetic dipole ($M_x^{(c)}$, $M_y^{(c)}$), magnetic toroidal dipole ($T_z^{(c)}$), and magnetic quadrupole ($M_{xy}^{(c)}$, $M_v^{(c)}$).

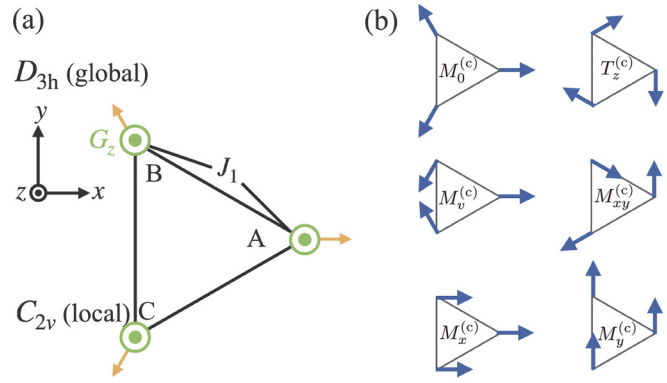

FIG. 10. (a) Three-site triangle cluster under the D_{3h} symmetry, where the site symmetry is C_{2v}. J_1 represents the exchange interactions between the nearest-neighbor sites. Yellow arrows represent the electric polarization $\boldsymbol{P}$, which originates from the potential gradient at each site. Green circles represent ETD moments along the z direction. (b) Six independent spin configurations in the three-site cluster: magnetic monopole ($M_0^{(c)}$), magnetic dipole ($M_x^{(c)}$, $M_y^{(c)}$), magnetic toroidal dipole ($T_z^{(c)}$), and magnetic quadrupole ($M_{xy}^{(c)}$, $M_v^{(c)}$). Blue arrows represent the spin moments at each site.

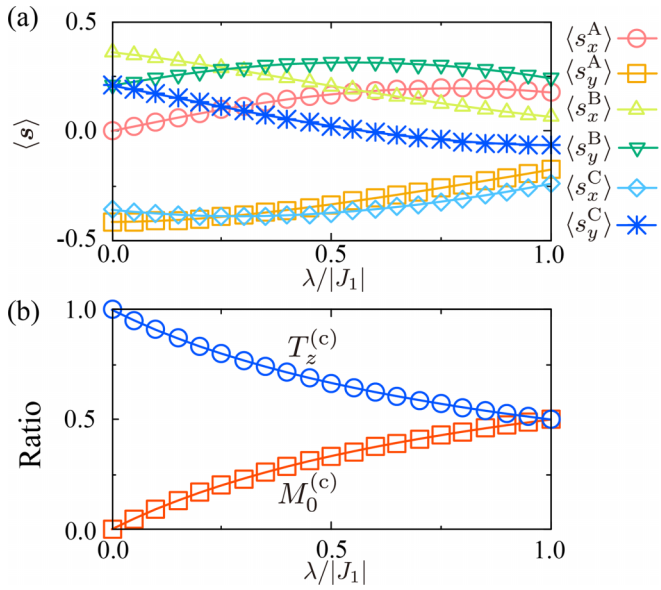

FIG. 11. SOC dependence of (a) spin moments on A, B, and C sublattices and (b) the ratio of $M_0^{(c)}$ and $T_z^{(c)}$ in the three-site model.

The spin configurations in each state are given by

$$M_0^{(c)} = (1, 0, -1/2, \sqrt{3}/2, -1/2, -\sqrt{3}/2), \quad \text{(E1)}$$

$$M_x^{(c)} = (1, 0, 1, 0, 1, 0), \quad \text{(E2)}$$

$$M_y^{(c)} = (0, 1, 0, 1, 0, 1), \quad \text{(E3)}$$

$$T_z^{(c)} = (0, -1, \sqrt{3}/2, 1/2, -\sqrt{3}/2, 1/2), \quad \text{(E4)}$$

$$M_{xy}^{(c)} = (0, 1, \sqrt{3}/2, -1/2, -\sqrt{3}/2, -1/2), \quad \text{(E5)}$$

$$M_v^{(c)} = (1, 0, -1/2, -\sqrt{3}/2, -1/2, \sqrt{3}/2), \quad \text{(E6)}$$

where the basis is represented by $(\sigma_x^A, \sigma_y^A, \sigma_x^B, \sigma_y^B, \sigma_x^C, \sigma_y^C)$. The real-space spin configurations in each case are shown in Fig. 10(b).

Figures 11(a) and 11(b) represent the spin moments at each site and the ratio of the spin configuration in the three-site triangle cluster for the nearest-neighbor antiferromagnetic exchange interaction $J_1 = -1$ and $h_G = 0.5$, respectively. We use the same CEF parameters for the A sublattice as those for the C sublattice in Appendix D. It is noted that the effect of the DM interaction is omitted. The CEF parameters in other sublattices are set to satisfy the C_3 symmetry. The results show a similar tendency as that of the four-site cluster in Sec. III. For $\lambda = 0$, the spin configuration is characterized by $T_z^{(c)}$. With the increase of λ, the spin moments gradually tilt, and the spin configuration is represented as a linear combination of $M_0^{(c)}$ and $T_z^{(c)}$. Thus, the effect of the ferroaxial moments on the magnetic instability is qualitatively similar to tetragonal and triangle models to each other, which implies the general aspect in terms of the magnetic instability under the ferroaxial moment.

[1] I. Dzyaloshinsky, J. Phys. Chem. Solids **4**, 241 (1958).
[2] T. Moriya, Phys. Rev. **120**, 91 (1960).
[3] N. Nagaosa and Y. Tokura, Nat. Nanotechnol. **8**, 899 (2013).
[4] G. Jackeli and G. Khaliullin, Phys. Rev. Lett. **102**, 017205 (2009).
[5] S. M. Winter, A. A. Tsirlin, M. Daghofer, J. van den Brink, Y. Singh, P. Gegenwart, and R. Valentí, J. Phys.: Condens. Matter **29**, 493002 (2017).
[6] M. Becker, M. Hermanns, B. Bauer, M. Garst, and S. Trebst, Phys. Rev. B **91**, 155135 (2015).
[7] L. Janssen, E. C. Andrade, and M. Vojta, Phys. Rev. Lett. **117**, 277202 (2016).
[8] X. Yao and S. Dong, Sci. Rep. **6**, 26750 (2016).
[9] T. Kaplan, Z. Phys. B **49**, 313 (1983).
[10] L. Shekhtman, A. Aharony, and O. Entin-Wohlman, Phys. Rev. B **47**, 174 (1993).
[11] R. Yambe and S. Hayami, Phys. Rev. B **106**, 174437 (2022).
[12] J. Ye, Y. B. Kim, A. J. Millis, B. I. Shraiman, P. Majumdar, and Z. Tešanović, Phys. Rev. Lett. **83**, 3737 (1999).
[13] K. Ohgushi, S. Murakami, and N. Nagaosa, Phys. Rev. B **62**, R6065 (2000).
[14] G. Tatara and H. Kawamura, J. Phys. Soc. Jpn. **71**, 2613 (2002).
[15] N. Nagaosa, J. Sinova, S. Onoda, A. H. MacDonald, and N. P. Ong, Rev. Mod. Phys. **82**, 1539 (2010).
[16] Y. Tokura and N. Nagaosa, Nat. Commun. **9**, 3740 (2018).
[17] C. Xiao, Z. Z. Du, and Q. Niu, Phys. Rev. B **100**, 165422 (2019).
[18] S. Hayami and M. Yatsushiro, Phys. Rev. B **106**, 014420 (2022).
[19] A. Kirikoshi and S. Hayami, Phys. Rev. B **107**, 155109 (2023).
[20] J. Hlinka, J. Privratska, P. Ondrejkovic, and V. Janovec, Phys. Rev. Lett. **116**, 177602 (2016).
[21] R. D. Johnson, L. C. Chapon, D. D. Khalyavin, P. Manuel, P. G. Radaelli, and C. Martin, Phys. Rev. Lett. **108**, 067201 (2012).
[22] W. Jin, E. Drueke, S. Li, A. Admasu, R. Owen, M. Day, K. Sun, S.-W. Cheong, and L. Zhao, Nat. Phys. **16**, 42 (2020).
[23] T. Hayashida, Y. Uemura, K. Kimura, S. Matsuoka, M. Hagihala, S. Hirose, H. Morioka, T. Hasegawa, and T. Kimura, Phys. Rev. Mater. **5**, 124409 (2021).
[24] T. Hayashida, Y. Uemura, K. Kimura, S. Matsuoka, D. Morikawa, S. Hirose, K. Tsuda, T. Hasegawa, and T. Kimura, Nat. Commun. **11**, 4582 (2020).
[25] H. Yokota, T. Hayashida, D. Kitahara, and T. Kimura, npj Quantum Mater. **7**, 106 (2022).
[26] T. Hasegawa, W. Yoshida, K. Nakamura, N. Ogita, and K. Matsuhira, J. Phys. Soc. Jpn. **89**, 054602 (2020).
[27] H. Hanate, T. Hasegawa, S. Hayami, S. Tsutsui, S. Kawano, and K. Matsuhira, J. Phys. Soc. Jpn. **90**, 063702 (2021).
[28] S. Hayami, S. Tsutsui, H. Hanate, N. Nagasawa, Y. Yoda, and K. Matsuhira, J. Phys. Soc. Jpn. **92**, 033702 (2023).
[29] H. Hanate, S. Tsutsui, T. Yajima, H. Nakao, H. Sagayama, T. Hasegawa, and K. Matsuhira, J. Phys. Soc. Jpn. **92**, 063601 (2023).
[30] X. Xu, F.-T. Huang, A. S. Admasu, M. Kratochvílová, M.-W. Chu, J.-G. Park, and S.-W. Cheong, Phys. Rev. B **105**, 184407 (2022).
[31] S.-W. Cheong, S. Lim, K. Du, and F.-T. Huang, npj Quantum Mater. **6**, 58 (2021).

[32] S. Hayami, R. Oiwa, and H. Kusunose, J. Phys. Soc. Jpn. **91**, 113702 (2022).
[33] A. Roy, M. H. D. Guimarães, and J. Sławińska, Phys. Rev. Mater. **6**, 045004 (2022).
[34] J. Nasu and S. Hayami, Phys. Rev. B **105**, 245125 (2022).
[35] A. Inda and S. Hayami, J. Phys. Soc. Jpn. **92**, 043701 (2023).
[36] S. Hayami, R. Oiwa, and H. Kusunose, Phys. Rev. B **108**, 085124 (2023).
[37] A. Kirikoshi and S. Hayami, J. Phys. Soc. Jpn. **92**, 123703 (2023).
[38] S. Hayami and H. Kusunose, J. Phys. Soc. Jpn. **87**, 033709 (2018).
[39] H. Watanabe and Y. Yanase, Phys. Rev. B **98**, 220412(R) (2018).
[40] H. Watanabe and Y. Yanase, Phys. Rev. B **98**, 245129 (2018).
[41] N. A. Spaldin, M. Fiebig, and M. Mostovoy, J. Phys.: Condens. Matter **20**, 434203 (2008).
[42] J. Hlinka, Phys. Rev. Lett. **113**, 165502 (2014).
[43] S. Hayami, M. Yatsushiro, Y. Yanagi, and H. Kusunose, Phys. Rev. B **98**, 165110 (2018).
[44] H. Kusunose, R. Oiwa, and S. Hayami, J. Phys. Soc. Jpn. **89**, 104704 (2020).
[45] M. Yatsushiro, H. Kusunose, and S. Hayami, Phys. Rev. B **104**, 054412 (2021).
[46] H. Kusunose and S. Hayami, J. Phys.: Condens. Matter **34**, 464002 (2022).
[47] G. Chen, R. Pereira, and L. Balents, Phys. Rev. B **82**, 174440 (2010).
[48] M.-T. Suzuki, T. Nomoto, R. Arita, Y. Yanagi, S. Hayami, and H. Kusunose, Phys. Rev. B **99**, 174407 (2019).
[49] S. Hayami, Phys. Rev. B **106**, 144402 (2022).
[50] S. Hayami and R. Yambe, Phys. Rev. B **105**, 104428 (2022).